

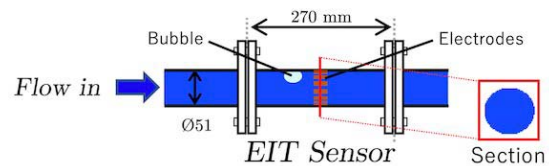
# High Speed EIT With Multifrequency Excitation Using FPGA and Response Analysis Using FDM

Mathieu Darnajou<sup>1</sup>, Antoine Dupré<sup>1</sup>, Chunhui Dang, Guillaume Ricciardi, Salah Bourennane, Cédric Bellis, and Saba Mylvaganam

**Abstract**—The investigation of quickly-evolving flow patterns in high-pressure and high-temperature flow rigs is crucial due to inherent hazards. There is a dire need for a high-speed, non-intrusive imaging technique to identify characteristic flow phenomena to alleviate these hazards. Electrical Impedance Tomography (EIT) enables reconstruction of the admittivity distribution of the flowing medium(s), facilitating the characterisation of its/their flow. The requirement for images at high frame-rates led to simultaneous voltage excitations over electrodes on the periphery of the flow associated to Frequency Division Multiplexing (FDM), doped ONE Excitation for Simultaneous High-speed Operation Tomography (ONE-SHOT) method. In previous studies, we have demonstrated the possibility of the full implementation of simultaneous excitations and measurements strategies for EIT, which maximise the number of measurements for 16 electrodes. This article presents the details of the proposed method and the signal generation/acquisition firmware based on a Field Programmable Gate Array (FPGA) data acquisition system focusing on hardware and software integration and the signal processing involved in realising the ONE-SHOT operation of the EIT. It is shown that the simultaneously generated signals are successfully discriminated and used for image reconstruction, at a rate up to 3906 frames per second (fps). The associated signal-to-noise ratio varies in the 55.6 dB–69.1 dB range, depending on the generated frequency in the range of 3.906 kHz–468.7 kHz.

**Index Terms**—Electrical impedance tomography, two-phase flow, frequency division multiplexing, FPGA, ONE-SHOT, real-time.

## EIT IMAGES AT 3906 FRAMES PER SECOND



## I. INTRODUCTION

IN THE context of high-pressure and high-temperature flow rigs, the timely identification of flow patterns helps by alerting the process engineers about hazardous situations

Manuscript received February 21, 2020; revised March 27, 2020; accepted March 27, 2020. Date of publication March 31, 2020; date of current version July 6, 2020. This work was supported in part by the Research Council of Norway and the Process Industries through the Project Self Adapting Model-based system for Process Autonomy (SAM) under Project 295945. The associate editor coordinating the review of this article and approving it for publication was Dr. Marko Vauhkonen. (Corresponding author: Mathieu Darnajou.)

Mathieu Darnajou and Chunhui Dang are with CEA-DES-IRESNEDTN Cadarache, F-13108 Saint-Paul-Lez-Durance, France, and also with the École Centrale de Marseille, 13013 Marseille, France (e-mail: mathieu.darnajou@centrale-marseille.fr).

Antoine Dupré is with SenTec AG, EIT Branch, CH-7302 Landquart, Switzerland.

Guillaume Ricciardi is with CEA-DES-IRESNEDTN Cadarache, F-13108 Saint-Paul-Lez-Durance, France.

Salah Bourennane is with the École Centrale de Marseille, 13013 Marseille, France.

Cédric Bellis is with Aix-Marseille Université, CNRS, Centrale Marseille, LMA UMR 7031, 13007 Marseille, France.

Saba Mylvaganam is with the Department of Electrical Engineering, IT and Cybernetics, Faculty of Technology, Natural Sciences and Maritime Sciences, University College of Southeast Norway, 3901 Porsgrunn, Norway.

Digital Object Identifier 10.1109/JSEN.2020.2984388

involving fast moving slugs or bubbles. Especially in applications involving extreme process conditions in the flowing medium, Electrical Impedance Tomography (EIT) [1]–[5] is a suitable non-intrusive technique for interrogating the medium continuously.

EIT consists of injecting (resp. measuring) electric currents through a set of electrodes at the surface of volume under observation and measuring (resp. injecting) the electrical potential over another set of electrodes. The standard excitation strategy uses Time Division Multiplexing (TDM), in which the excitation signal is routed to a single selected pair of electrodes at any given time. The sequential selection of these pairs of electrodes with multiplexers or electronic switching [6] creates an excitation strategy producing an EIT data frame, which includes the measurement data for all excitation pairs [7]. The EIT data can be used in the solution of the potential distribution with Neumann and Dirichlet boundary conditions to solve the associated inverse problem of reconstructing the distribution of material properties such as the electric conductivity, permittivity etc. in the meter-head containing the fluids under test.

EIT requires data acquisition for high frame rate, for instance in flow studies involving quickly-evolving flow

regimes [8], [9]. In such conditions and using TDM, high speed is reached using a small number of electrodes, a partial scanning strategy, or short measurement times, often with a combination of these [10]–[15]. A solution for increasing the acquisition rate of EIT is to perform simultaneous electrical excitations and measurements at the surface electrodes, leading to a superposition of signals in the acquisition channels.

Based on simultaneous multifrequency stimulations, the overlapping signals can be identified individually using Frequency Division Multiplexing (FDM) [16]–[18]. In [19], a proof-of-principle experiment predicted the feasibility of the demodulation of simultaneous excitations with respect to their frequencies, based on a four-electrode EIT system. In [20], an experiment performed the generation and discrimination of 15 signals injected simultaneously on to a single electrode. The combined excitation signals with their simultaneous responses at the electrodes of the EIT module were used to produce images. These studies helped to establish the proof of concept of realising an EIT module using multifrequency excitation with FDM based detection of response signals without looking into the high-speed data acquisition.

Multifrequency EIT has been used in reconstructing the distribution of conductivity of the region of investigation by fusing the spatiotemporal data of tissue conductivity measured at different frequencies [21]–[26].

In Electrical Capacitance Tomography (ECT), another soft field technique, simultaneous excitation strategies have been applied in multiphase flow studies. [27]–[30].

Multifrequency tomography has been used in tomographic applications involving other sensor modalities, e.g. magnetic induction, acoustic and acousto-optic modalities. [31]–[33].

Multifrequency bioelectrical impedance analysis [34]–[37] was introduced mainly in medical applications and especially in sports medicine. Multiple frequency bioelectrical impedance analysis was used in obtaining bioimpedance data at several different frequencies for quantification of extracellular water at low but spot frequencies (1.0 kHz and 5.0 kHz), and total body water at higher spot frequencies (100 kHz, 200 kHz, or 500 kHz). Bioimpedance spectroscopy presented in the same study for bioimpedance measurements across a range of frequencies (5 kHz - 1000 kHz).

An interesting study describing numerical techniques relevant for anomaly distribution using multifrequency EIT is presented in [38].

The hardware, software used along with the hardware-software integration in these multifrequency EIT, ECT, other tomographic applications and bioimpedance measurements set-up are somewhat different to those presented in this article. The handling of the agglomerate of 120 excitation signals in this article and the detection of the response signals are also different to those presented in the earlier studies.

The present article describes the Field Programmable Gate Array (FPGA) and Real Time (RT) software solutions to implement the full excitation and measurement strategy of the ONE Excitation for Simultaneous High-speed Operation Tomography (ONE-SHOT) method [19], [20]. The details of the high speed data acquisition system are presented in

Section II. Section III focuses on the hardware configuration needed for the high speed data acquisition. Section IV presents the multifrequency signal generation strategies, which is followed by Section V dealing with signal acquisition. These two sections includes the details on the firmware structure. The details on the output data format is discussed in Sec. VI. Moreover, experimental results, including data, noise analysis and image reconstruction are discussed in Sec. VII. Finally, Section VIII deals with the spectral analysis. An electrode model for the contact impedance analysis is proposed in Section IX.

## II. RESEARCH OBJECTIVES

The goal of this research is to achieve high speed acquisition of data frames for imaging of multiphase flow. Each frame contains the maximum number of linearly independent excitations and measurements for a given set of 16 electrodes, using a set of multifrequency signals for the excitation of 16 electrodes. From the state of the art along with the findings of our own work presented in [20], three major areas need to be addressed for improved performance in achieving this high-speed data acquisition:

### A. Analog Signal Generation

The first aspect is the generation of continuous signals at 120 distinct frequencies. An important task in this process is the selection of suitable frequencies for good performance of the FDM. A possible solution according to [39], [40] is to generate harmonics based on Fast Fourier Transform (FFT) frequency components and their amplitudes matching the frequencies/amplitudes of the generated frequencies. This solution results in a large bandwidth for 120 frequencies, while the signal frequencies are restricted by the Nyquist sampling limit determining the proper detection of the signals at the sensing electrodes. Moreover, harmonics of low frequency interfere with the signals in the upper frequency range, as discussed in [41]. We need to address effects of the available bandwidth on the possible data acquisition rates. An alternative scheme for signal generation based on periods based on prime numbers is also presented.

The determination of the signal amplitudes is based on experimental observations. The Data Acquisition (DAQ) system used in our experiments operates within  $\pm 10$  V for Analogue Outputs (AO), [20], [42]–[44]. The simultaneous generation of the 120 signals implies large values for the temporal derivative of the voltages ( $dV/dt$ ), imposing restrictions on the output voltage levels in the DAQ system. We discuss, based on experimental observation, methods of maximising the signal output voltage to increase the Signal to Noise Ratio (SNR) while keeping good discrimination of the signals at different frequencies for implementing the FDM.

Moreover, the firmware is extended from 15 frequencies to 120 frequencies using a larger Block Random Access Memory (BRAM), which is beyond the capacity of single FPGA chip, given the implementation strategy described in [20]. There are at least two solutions for extending the capacity of the FPGA. An array of FPGA chips can be used to

increase the BRAM. First option enabling the fast operation for high frames per seconds (fps) necessitates a robust and fast synchronisation strategy, as discussed in [45]. Second option is the generation of the signals point by point from a pre-computed Look-Up-Table (LUT), saved in the FPGA. The second option using the LUT saved in the FPGA is adopted here. For achieving the high-speed operations, LUTs are integrated in the FPGA firmware. This gives no flexibility in selecting the signal generation patterns, once the firmware is compiled. We propose to use one LUT for two AO channels. By using two accumulators incremented in a loop at high speed, we were able to extract two signals at two different frequencies from the same LUT. This strategy permits the firmware to fit into a single FPGA chip while keeping the same flexibility for the signal generation.

### B. Analog Signal Acquisition

The second task is to build a firmware architecture to acquire 16 analog signals in parallel and apply FFT at the high rate of 1 Mega Samples per second (MS/s). The full implementation of the ONE-SHOT method requires each FFT operation to extract 120 Fourier coefficients per channel. In this architecture, we associate parallel FFT computing and large data transfer, based on Direct Memory Access (DMA), like the work described in [46].

### C. Output Data Format

The excitations are based on the association of positive and negative sinusoidal signals used for excitation. The signs of the magnitudes are usually determined from the phase of the Fourier transforms. However, the phase-shift of the signal spreading in the domain is potentially large, creating phase wrapping effects. A solution proposed by [47] is to extract the wrapped phase in image processing with Gabor filter. However, in EIT, the discretisation from the electrodes creates large phase discontinuities and the Gabor filtering cannot be used. In this article, we bring a novel solution, based on an intuitive estimation based on the sign matrix of the measured Fourier coefficients.

Finally, the full implementation of the ONE-SHOT method at maximum rate necessitates high performance data buffer to handle up to 75 MB/s of data. This requirement of the data buffer led to the implementation of a high-performance data storage system.

## III. MATERIAL TO IMPLEMENT THE ONE-SHOT METHOD

The ONE-SHOT method uses simultaneous excitation signals at several frequencies, on each electrode to increase the data frame rate and eliminate transients at the electrode-electrolyte interface. In parallel, FDM is performed by point-by-point synchronous Fourier transforms, implemented on FPGA to optimise the data acquisition speed. The excitation pattern is described in detail in [20].

This article focuses on signal processing based on the DAQ system which is composed of three elements:

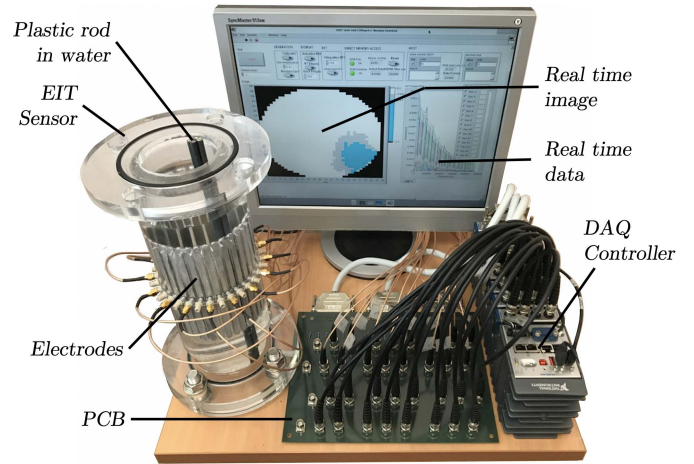


Fig. 1. The system implementing the ONE-SHOT method as used for static experiment. The EIT sensor is filled with water and a plastic rod of low conductivity is inserted to mimic non-conductive inclusions. The software provides a 2D real time image of the probed medium.

- **The EIT sensor:** contains a set of 16 electrodes (Fig. 1) tangential to the inner surface of the pipe and in contact with the fluid. The electrodes are used for excitation and measuring the response of the medium.
- **The Printed Circuit Board (PCB):** used for the 16 excitation signals fed to the 16 electrodes. The material distribution is estimated using reconstruction algorithms from voltage measurements over 16 resistors on the PCB.
- **The DAQ controller:** manages both AO excitations and Analog Input (AI) measurements. This task is achieved using the National Instruments CRIO-9039 [42] which includes the Xilinx's Kintex-7 325T FPGA [48]. The DAQ controller provides 16 voltage AO channels provided by NI-9262 AO modules [43] and 16 voltage AI channels NI-9223 AI module [44]. All channels are operated at 1 MS/s.

## IV. ANALOG SIGNAL GENERATION

In [20], we demonstrated the feasibility of discriminating 15 voltage signals, simultaneous pairwise excitation of 16 electrodes. The implementation of the ONE-SHOT method in an EIT module with 16 electrodes requires a set of 120 signals of different frequencies. The complexity for generating a large number of frequencies is balanced by the benefit of a full set of excitation pairs which increases in turn the well-posedness of the inverse problem for a given number of electrodes. In the following, we discuss in Sec. IV-A, the requirements on the frequencies and the constraints for the generation of the signals. Sec. IV-B concerns the amplitude of the generated sinusoidal signals. Finally, Sec. IV-C details the firmware structure.

### A. Excitation Frequencies

The discrimination of the excitation signals is achieved using FFT. The number of points considered for the FFT as well as the sampling frequency of the DAQ system suggest the following restrictions on the generated signals.

Firstly, the Nyquist sampling theorem limits the highest usable output frequency. In practice, to avoid aliasing or harmonics noise and ensure the quality of the output signal, the minimum number of samples in a single sinusoid period to compute the FFT is two. For the acquisition system operated at  $f_{acq} = 1$  MS/s, the theoretical maximum excitation/acquisition frequency is the Nyquist limit:  $f_{Nyq} = f_{acq}/2 = 500$  kHz for a DAQ system operated at 1 MS/s.

Secondly, the residual voltage resulting from the energy stored in the electrode-electrolyte contact impedance is a great source of error in EIT [49]–[51]. However, if a continuous signal is generated, the spurious signals due to contact impedances are eliminated. The solution is to chose the lowest generated signal frequency  $f_1$  to be equal to the FFT computation frequency, which depends on the number of integrated samples. The other frequencies are then chosen such that an entire number  $k \in \mathbb{N}$  of periods fits inside  $f_1$ . Thus,  $k$  is the absolute Fourier coefficient as well as the harmonic index and is associated to the frequency  $f_k = kf_1$ . Note that the FFT magnitude does not depend on the phase shift, which is an advantage.

In an early stage of the implementation of the ONE-SHOT method, only prime numbers of sinusoid period were considered in order to avoid resonances from lower to higher frequencies. Experimentally, the amplitude of the resonance peaks were measured to be about 1% of the fundamental harmonics. In the current system that excites the 120 independent pairs of electrodes at 120 frequencies, the 120<sup>th</sup> prime number, 661, gives a generated sinusoid frequency of 1.2 MHz (0.60 MHz) for an FFT over 512 points (1024 points), which is beyond the maximal frequency  $f_{Nyq}$ . Furthermore, the 661<sup>th</sup> resonance of an FFT computed over 2048 points is 0.20 MHz and this option could be considered to avoid effects of harmonics in the measurements. The frame rate in the last case is 488 fps which, for 16 electrodes, is the typical rate of the available fast EIT systems based on TDM.

### B. Excitation Amplitudes

The voltage generation and acquisition modules are constrained within the range  $\pm 10$  V. Considering the generation patterns given in [20], the amplitude  $A$  of the sinusoids must be much lower than the generated sum of sinusoids due to constructive interferences between them. On the other hand, the signal amplitude must remain as large as possible in order to reduce the SNR.

Another limit is the maximum variation allowed between two successive generated voltages. A real-time control in the DAQ system allowed to set the adequate value of  $A = 0.15$  V, giving resonance peaks at  $\pm 2.25$  V. The fast transition between negative and positive signal values cancels the apparition of electrolytic effects [19], [51].

### C. Firmware Structure

This section details the coding strategy for managing the excitation signals. We give an overview of the software logic blocks, step by step.

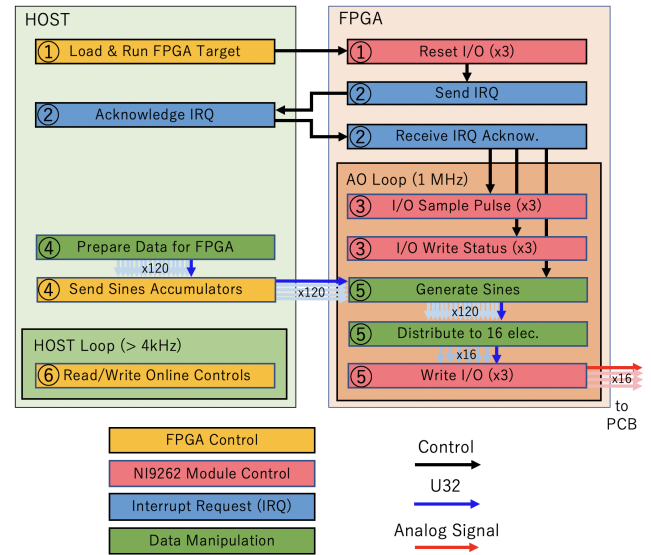


Fig. 2. Layout of AO Logic. The colours of the boxes and arrows indicate respectively the nature of the functions used and the formats of the data transfer.

The LabVIEW code for the generation and distribution of the 120 sinusoids of different frequencies is based on two levels: Host and FPGA. While the Host sends continuously the frequencies and amplitude parameters to the FPGA, the latter takes the data points 16 by 16 in a loop cadenced at the high rate of 1 MS/s to create 16 analog signals. The following details the firmware structure including the layout of the LabVIEW based AO logic in Fig. 2.

- ① When starting the execution, the FPGA is blank and requires the information to structure itself. The *Load and Run FPGA Target* function is implemented by the Host prior to call the *Reset I/O* function of the three AO modules. When this call completes, the FPGA is ready to perform the other functions for the AO modules control.
- ② The acquisition of the data has to be ready before generating any signal. An Interrupt Request (IRQ) is used to warn the Host that the FPGA is ready to begin acquiring data and is waiting to start the acquisition until the Host acknowledges it. This is necessary to ensure that the DMA First-In-First-Out (FIFO) in the acquisition firmware (see Sec. V) has been started.
- ③ Call the *Generate Sample Pulse* function to start generating data points. The rate at which the function is called determines the sampling rate for the generation, so that a loop timer is used to enforce the desired sampling period of 1 MS/s. In parallel, the *Write I/O Status* function is called at the same rate to check the status of every generated sample. If an overwrite occurs, the generation is stopped and an error message is reported to the Host.
- ④ The Host *Prepare Data for FPGA* contains two functions: *Generate Harmonic Parameters*, *Generate Sines Parameters*. As discussed in Sec. IV-A, the frequencies of the generated signals are harmonics of the FFT frequency. To ensure an accurate correspondence, the 120 frequencies are set up using integers, representing the order of

the harmonics  $k$  of the fundamental frequency. In the next step, the function *Generate Sines Parameters* uses Direct Digital Synthesis (DDS) to translate the harmonic numbers into 120 sinusoids accumulator increments at the Unsigned 32-bits (U32) format for the FPGA. The function also provides the amplitude calibration of the AO modules by setting the adequate scaling parameters. To ensure that the FPGA loop starts after receiving the values from the accumulators, these are sent to the FPGA prior acknowledging the IRQ.

- ⑤ Each U32 accumulator contains 13 bits to address the 8192 elements stored in a LUT, saved on the FPGA chip. The LUT outputs the addressed element, linearly interpolated between one address and the next one, given by the 16 remaining bits of the U32 accumulator. The LUT returns an 16-bits Integer (I16) by truncating the fractional bits resulting from the interpolation operation. The obtained value is scaled with the signal amplitude. There is a total of 240 positive and negative sinusoidal signals that are dispatched to the 16 electrodes. To avoid a large BRAM on the FPGA, only 60 LUTs are stored on the FPGA. Each LUT is read in a loop at 2 MHz and two values are extracted independently at 1 MHz from two accumulators. The benefit is to control individually the channels in RT, without necessitating a renewed compilation of the firmware.
- ⑥ The Host contains online control functions to confirm that signals are generated, to report loop iteration speed and to report eventual errors at Host or FPGA levels in RT.

## V. ANALOG SIGNAL ACQUISITION

The measurement of voltages over resistors on the PCB gives access to Neumann boundary conditions for the image reconstruction algorithm. The high rate acquisition at 1 MS/s over 16 channels corresponds to a large data transfer rate of 320 MB/s. We found two positive aspects in using FFT: the first is to reduce the data size without altering the data quality by considering only the Fourier coefficients that are related to a generated signal. The second is to act as an efficient bandpass filter. However, the computation of 16 FFTs online requires very high speed computations. The FPGA is a suitable device for this task since it allows the online and parallel transformation of the signals into its Fourier components over multiple channels.

This section details the coding strategy used for the task of acquiring the signals and transforming them into their FFT components. The Host generation functions ①, ② and ⑥ are also used to monitor the acquisition. The AO and AI FPGA firmwares are implemented together on the single FPGA chip and run in parallel.

The following details the algorithm scheme of Fig. 3:

- Ⓐ The *Load and Run FPGA Target* is shared with the AO logic. In parallel to the AO firmware, the FPGA calls the *Reset I/O* function of the four AI modules. Once this function is called, the AI modules are ready to acquire analog signals and proceed to their digitalisation.
- Ⓑ The large AI data transfer from the FPGA to the Host is based on a DMA strategy. At the very start of the

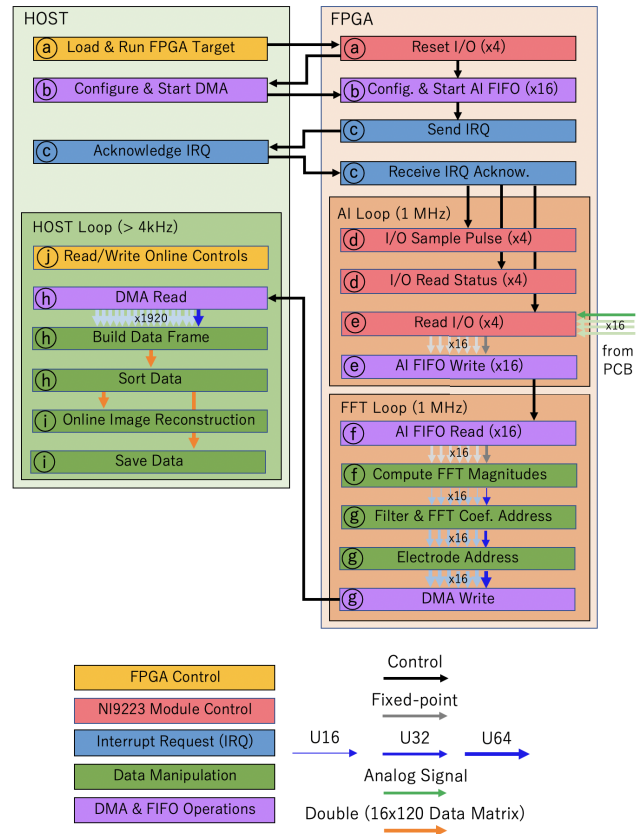


Fig. 3. Layout of AI Logic representing the Host software, shared with the AO and the FPGA firmware including two loops operating in parallel at 1 MHz. The colours of the boxes and arrows indicate respectively the nature of the functions used and the formats of the data transfer.

compilation, the Host *Configures and starts the DMA*. Subsequently, the FPGA *Configures and starts the AI FIFOs*. These 16 FIFOs are used to ensure the communication from the 16 measurement channels to their FFT computations.

- Ⓒ As in the AO firmware, the IRQ is used to ensure that the DMA and AI FIFOs are ready before generating and acquiring data.
- Ⓓ By analogy with the AO modules, the *Generate Sample Pulse* function is called to control the sampling rate. In parallel, the *I/O Read Status* is called at the same rate to check the status of every acquired sample and report an eventual error to the host.
- Ⓔ The *Read I/O* function is configured to read a single sample from each channel on each AI module. This function is called at 1 MHz and regulated by the *Generate Sample Pulse* function.
- Ⓕ The FFT of each channel is computed in a loop operated at the iteration speed of 1 MHz, as the AI loop. The computation time is managed by the number  $P$  of points considered for the FFT. Once all the  $P$  measurement data points sequence is transferred for FFT computations, the function outputs the  $P$  Fourier coefficients one by one at each iteration of the FFT loop. In a second step, the magnitude of the FFT coefficients are computed at a rate of 1 MHz.

- Ⓒ The extraction of the data through FFT acts as an efficient bandpass filter since only the harmonics of the FFT computation time are considered. Each data point magnitude is of format U32 and addressed with the corresponding Fourier coefficient and channel both at the format 16-bits Unsigned integer (U16). The association creates an addressed 64-bits Unsigned integer (U64) data element. At each iteration of the FFT loop, 16 elements for the 16 channels are written in the DMA to be transferred to the host computer. More details on the data format will be introduced in Sec. VI.
- Ⓓ The Host waits for the DMA to collect at least 1920 elements representing one full data frame. The address of the  $n^{th}$  electrode and the Fourier coefficient associated with the FFT magnitude  $M$  are used to build a data matrix denoted as  $D$ .
- Ⓔ The data are either used for online image reconstruction or stored. The image is based on the one step least square iterative reconstruction algorithm [52], [53], implemented using a MATLAB interface in LabVIEW. The computation time is much slower than the data frame rate obtained with the ONE-SHOT method. Online imaging can be achieved at around a hundred of frames per seconds. For this reason, the data are stored independently in a binary file to assure fast operation.
- Ⓕ As in the signal generation step, the firmware reports errors and checks the synchronisation of AO and AI.

## VI. OUTPUT DATA FORMAT

In EIT, the data for one measurement are a set of points describing the sinusoidal voltage over one or several periods. However, in practice, only the magnitude of the signal is of importance and the data size can be significantly reduced in the post processing. The computation of the FFT within the FPGA has two additional advantages: Firstly, the output data matrix contains only the magnitudes and its size is significantly reduced. Secondly, the magnitudes of the Fourier coefficients not corresponding to an excitation signal frequency are discarded. This section discusses first a single standard EIT measurement data followed by the full set of measurements case. Then, the ONE-SHOT method dataset developed in [19], [20] is recalled, detailing the advantages of using a FPGA-based system for the measurements.

### A. Standard EIT Data

In TDM EIT, a single measurement (Fig. 4) is the association of a single excitation pair of electrodes  $E_{n,m}$  for  $1 \leq n \leq n_e$ ,  $1 \leq m \leq n_e$  and  $n \neq m$  with a single pair of measurement electrodes. The signal is typically a sinusoidal signal of frequency  $f$ , recorded over a finite number of periods  $n_p$ . The acquisition signal contains a finite number of points, recorded over a time  $n_p/f$ , at the rate equal to the acquisition frequency  $f_{acq}$  which is constrained by the hardware system.

A single measurement dataset contains

$$S_{single} = f_{acq} \frac{n_p}{f} \quad (1)$$

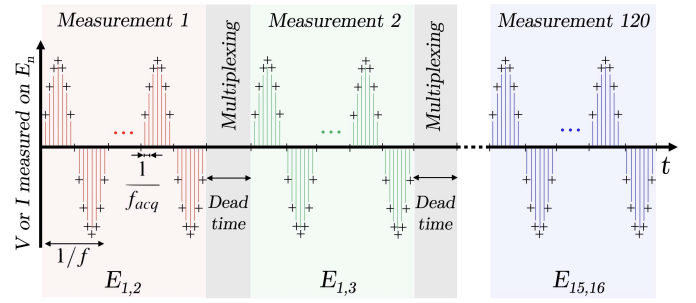


Fig. 4. Representation of a full dataset for the standard TDM EIT acquisition process for 16 electrodes. The full dataset contains 120 single measurements, and here, only three are shown. The dead time dedicated to multiplexing is usually longer than the above representation.

measurement points, typically 10 to 100. The measurement over each electrode gives a similar dataset for the total number  $n_e$  of electrodes.

A large measurement set improves the inverse problem conditioning for image reconstruction. Therefore, maximising the number of measurements improves the description of the boundary conditions for a given set of electrodes. For an EIT system with  $n_e$  electrodes, there is two ways to maximise the number of measurement. Firstly, by considering excitations between the  $N$  independent pairs of electrodes with

$$N = \frac{n_e (n_e - 1)}{2}. \quad (2)$$

Secondly, by considering measurements over every electrode, as shown in Fig. 4.

Therefore, from equations (2) and (1), the total number of elements for all excitations and measurements is:

$$S_{TDM} = S_{single} n_e N = \frac{f_{acq} n_p n_e^2 (n_e - 1)}{2f} \quad (3)$$

Here, the number of points per measurement  $S_{single}$  is systematically reduced to 1 in the image reconstruction step, where only the amplitude of the Fourier transform is used.

In addition, in order to reduce the error due to contact impedance effects, the TDM based excitation strategy requires dead time between successive excitations [15], when selecting another pair of excitation electrodes.

### B. Data From FPGA Based ONE-SHOT Method

On the other hand, the association of FDM with the appropriate FPGA firmware strategy allows to keep only the Fourier magnitudes of interest. The FPGA based FFT permits an online spectral analysis over 16 channels at the rate of 1 MS/s.

The FFT is computed from a  $P$ -point voltage measurement sequence  $\{V_n(p)\}$  with  $p$  the discrete time and  $0 \leq p \leq P$ . The data points are the magnitudes of the Fourier coefficients in the  $n$ -electrode channel; i.e.

$$M_n(k) = \frac{1}{P} \left| \sum_{p=0}^{P-1} V_n(p) e^{ik\beta p} \right| \quad (4)$$

with  $\beta_p = 2\pi p/P$ ,  $i = \sqrt{-1}$  and a synchronous sampling is assumed.

Each 32-bits magnitude data point  $M_n(k)$  is assigned with the corresponding 16-bits Fourier coefficient and 16-bits  $n$ -electrode address as:

$$M_n(k) = \underbrace{16 \text{ bits}}_k + \underbrace{16 \text{ bits}}_n + \underbrace{32 \text{ bits}}_M \quad (5)$$

The data format of each element is then a U64. Theoretically, for 16 electrodes, it could be possible to reduce the data size by considering only 8-bits for the Fourier coefficients and 4-bits for the electrode address. The number of bits allocated to the FFT magnitude must take into account the precision of the FFT reconstruction, which depends on the FFT integration time. The 16 + 16 + 32 bits data format is considered in this article for future developments of the ONE-SHOT method for 32 electrodes.

The 16 magnitudes measured on the 16 electrodes for a given Fourier coefficient  $k$  gives a data vector:

$$\{M_n(k)\} = (M_1(k) M_2(k) M_3(k) \dots M_{16}(k)) \quad (6)$$

where the  $M_n(k)$  are U64 elements as in (5). A data matrix  $\mathbf{D}$  then concatenates the set of magnitude vectors for the  $N$  Fourier coefficients corresponding to the  $N$  generated frequencies, i.e.:

$$\mathbf{D} = \begin{pmatrix} \{M_n(1)\} \\ \{M_n(2)\} \\ \{M_n(3)\} \\ \vdots \\ \{M_n(120)\} \end{pmatrix} \quad (7)$$

which constitutes a data frame. In this case, by analogy with (3) the data size is given by:

$$S_{FDM} = N n_e = \frac{n_e^2(n_e - 1)}{2} \quad (8)$$

where only the magnitudes of the Fourier transform are output, which reduces the data size by the factor of  $S_{single}$  in comparison with the TDM.

The FFT is computed at a frequency  $f_1$  from  $P$  data points, resulting in  $P$  Fourier coefficients at the output. The generated signals are of frequency  $f_k$  with  $1 \leq k \leq N$ , and are defined as harmonics of  $f_1$ . Therefore, each coefficient  $k$  is associated with a specific frequency value  $f_k$ . In this setting, the data frame rate is  $f_1$  and the resolution in the Fourier space is  $\Delta f = f_{k+1} - f_k = f_1$ . Considering the  $N$  independent pairs of electrodes for the excitations, the  $N^{th}$  harmonic of  $f_1$  is imposed below the Nyquist limit  $f_{Nyq}$  as discussed in Sec. IV-A. One solution consists in generating the firsts  $N$  harmonics of  $f_1$ , giving  $f_k = k f_1$ , for  $k = 1, \dots, N$ .

In addition, among all  $P$  Fourier coefficients, only the coefficients corresponding to the  $N$  generated signals are of interest. The magnitudes associated to a Fourier coefficient that are not related to a generated frequency are discarded.

Finally, one data frame  $\mathbf{D}$  of the ONE-SHOT method is represented in Fig. 5. With its elements in the format of (5),  $\mathbf{D}$  contains 123 kB of information. By comparison with TDM EIT systems, the benefits of the ONE-SHOT method associated with the FPGA implementation strategy is more data frames for an equivalent total data size.

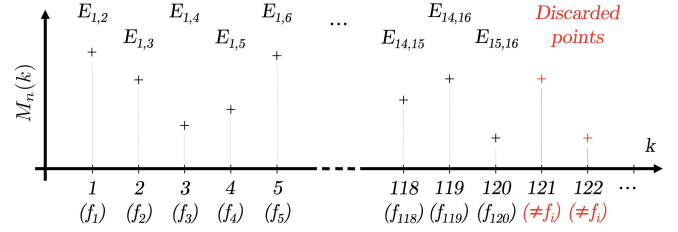


Fig. 5. Representation of the 120 data points considered in the ONE-SHOT method current measurement on a given electrode. All other magnitudes for any other Fourier coefficient  $k$  are discarded.

### C. Sign of the Signal Magnitudes

The phase shift  $\phi_n$  between the excitation signal and the measured signal at the  $n^{th}$  electrode depends on the frequency, the physical properties and material distribution of the probed medium. We consider the two following possibilities:

1) Case  $|\phi_n| < \pi/2$ : The sign of the measured magnitude can be determined from the sign of  $\sin(\phi_n)$  with:

$$\phi_n = \arctan \left( \frac{-\sum_{p=0}^{P-1} V_n(p) \sin(k\beta_p)}{\sum_{p=0}^{P-1} V_n(p) \cos(k\beta_p)} \right) \quad (9)$$

and we can define the signed data matrix  $\tilde{\mathbf{D}}$  with its elements given by:

$$\tilde{D}_n^k = \frac{\sin(\phi_n)}{|\sin(\phi_n)|} D_n^k \quad (10)$$

where  $D_n^k$  denotes the elements of  $\mathbf{D}$ , defined in (7).

2) Case  $|\phi_n| \geq \pi/2$ : The dependency on the frequency or on the distance between the electrodes affects the sign. In this case, experimental parameters affects drastically the images associated with a given flow pattern. A solution is proposed with the introduction of the sign matrix  $\Sigma$  to affect an arbitrary sign to the signals.

The sign of the magnitude on a given electrode is arbitrarily chosen as the sign of the same magnitude for an electrostatic excitation in a homogenous medium. In other words, the opposite sign of the closest excitation electrode. In the particular case of a measurement electrode at equal distance between two excitation electrodes, the amplitude is found experimentally to be of order  $O(10^{-7})$  A which is a negligible contribution to the data. To summarise, the  $n_e \times N = 16 \times 120$  sign matrix is defined as follows:

$$\Sigma = \begin{pmatrix} \oplus & \ominus & + & + & + & + & + & + & + & + & - & - & - & - & - & - & - & - \\ \oplus & - & \ominus & + & + & + & + & + & + & + & - & - & - & - & - & - & - & - \\ \oplus & - & + & \ominus & + & + & + & + & + & + & - & - & - & - & - & - & - & - \\ \oplus & - & - & + & \ominus & + & + & + & + & + & - & - & - & - & - & - & - & - \\ \oplus & - & - & + & + & \ominus & + & + & + & + & - & - & - & - & - & - & - & - \\ & & & & & & \vdots & & & & & & & & & & & & \\ + & + & + & + & + & + & - & - & - & - & - & - & - & - & \oplus & - & \ominus & \\ + & + & + & + & + & + & - & - & - & - & - & - & - & - & - & \oplus & \ominus \end{pmatrix} \quad (11)$$

with the + and - symbols representing respectively the numbers +1 and -1. The symbols  $\oplus$  and  $\ominus$  denotes respectively the source and the drain.

Finally, for a large phase shift,  $\tilde{\mathbf{D}}$  contains the arbitrarily signed amplitudes of the 120 excitation patterns for the

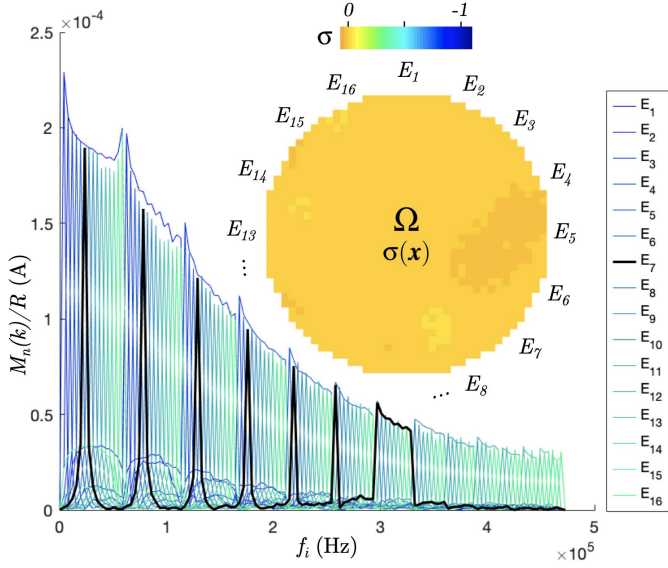


Fig. 6. Raw data from all of the 16 electrodes of a homogenous water medium of conductivity  $\sigma = 635 \mu\text{S}\cdot\text{m}^{-1}$ . The data from the electrode  $E_7$  are shown in black for comparison purposes with the next figure. In the upper-right corner, the image of the reconstructed electrical conductivity  $\sigma(x)$  with the arbitrary values  $0 \leq \sigma \leq 1$  is shown.

16 electrodes where the element corresponding to the  $k^{\text{th}}$  Fourier coefficient and the  $n^{\text{th}}$  electrode is:

$$\tilde{D}_n^k = \sum_n D_n^k \quad (12)$$

similar to (10).

## VII. EXPERIMENTAL RESULTS

The full implementation of the ONE-SHOT method is assessed on static experiments. The excitation software, the measurement software and the data format are these described in Sec. IV, Sec. V and Sec. VI, respectively. The following section introduces the measured data of two homogeneous and inhomogeneous static mediums in Sec. VII-A and Sec. VII-B, respectively. The results of a dynamic two-phase flow experiment are presented in Sec. VII-C. The SNR of the signals are discussed in Sec. VII-D.

### A. Static Homogeneous Medium

An experiment is set up to measure the system response from a homogeneous medium. The test section is filled with water of conductivity  $\sigma = 635 \mu\text{S}\cdot\text{m}^{-1}$  and a data frame is acquired. The data frame, with the same representation as in Fig. 5 for the 120 magnitudes data points measured on the 16 electrodes is shown in Fig. 6. The magnitudes are voltages measured over resistances on the PCB. The figure represents the measured current in Ampere, obtained from  $M_n(k)/R$  with  $R = 200 \Omega$ .

The generated signals frequencies  $f_k$  are chosen so as to maximise the image refresh rate. This is obtained by considering the FFT to be computed over  $P = 256$  data points at  $f_{acq} = 1 \text{ MS/s}$ , with  $f_1 = (256 \mu\text{s})^{-1} = 3906 \text{ Hz}$ . Considering 16 electrodes, then  $N = 120$  and the highest frequency is  $Nf_1 = 468.7 \text{ kHz}$ , which respects the Nyquist limit

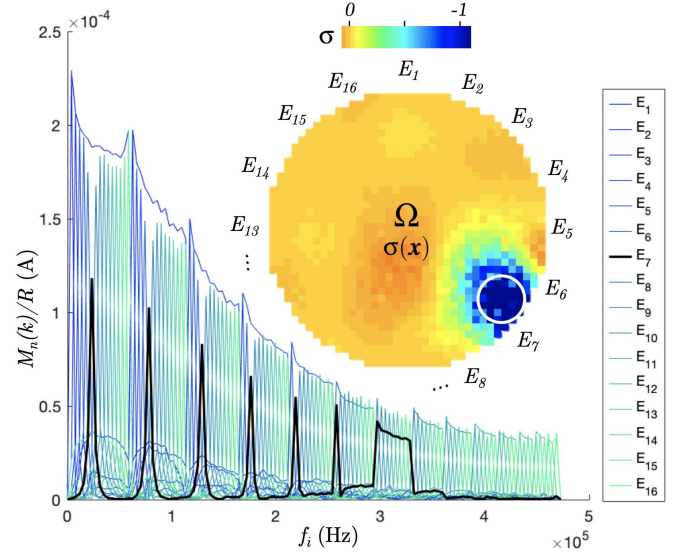


Fig. 7. Raw data for an inhomogeneous medium. The data from the electrode  $E_7$  are shown in black for comparison purposes with the Fig. 6. In the upper-right corner, the image of the reconstructed electrical conductivity  $\sigma(x)$  with the arbitrary values  $0 \leq \sigma \leq 1$  identifies the inclusion, shown with the white circle.

$f_{Nyq} = f_{acq}/2 = 500 \text{ kHz}$ . In this setting, the image refresh rate is maximised at 3906 fps with a full set of 1920 measurements per frame. It is important to point out that maximising the image refresh rate is at the price of a large bandwidth, i.e. a large difference between the lowest frequency  $f_1$  and the largest frequency  $f_{120}$ .

We observe that the signal magnitudes are well discriminated from one another. The magnitudes decrease at higher frequencies.

### B. Static Inhomogeneous Medium

The dataset of an inhomogeneous medium is shown Fig. 7. In this experiment, the test section is filled with the same water but includes a non-conducting PMMA rods of diameter 10 mm close to the electrode  $E_7$ , as shown in Fig. 1.

The comparison of Fig. 6 and Fig. 7 using the measured data from the electrode  $E_7$  shows the system response for different frequencies. We observe signals of lower magnitudes close to the inclusion on the electrode  $E_7$  and its neighbouring electrodes.

As an example, two images are reconstructed from the homogeneous and inhomogeneous data. The one-step least-squares iterative reconstruction method [52], [53] is implemented, and the results are shown in the upper-right corner of Fig. 6 and Fig. 7.

The images show the non-dimensional normalised variation to a reference image of the electrical conductivity  $\sigma(x)$  with  $x \in \Omega$ , where  $\Omega$  is the system representing the two dimensional median cross section of the 3D EIT sensor.

The variations in the conductivities are  $\sigma_{\max}(x) = 0.027$  for the homogeneous medium (Fig. 6) and  $\sigma_{\max}(x) = -1$  for the inhomogeneous medium (Fig. 7), in the close neighbourhood of electrode  $E_7$ .



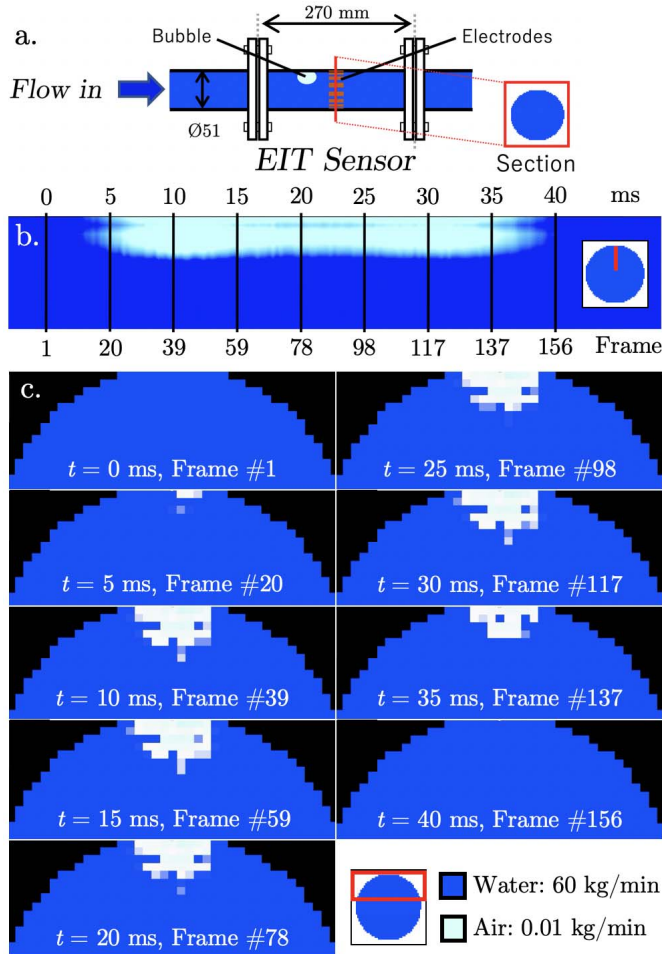


Fig. 8. a. Layout of the dynamic experiment. b. Longitudinal representation of the 156 reconstructed EIT images of an air bubble passing through the pipe section with the electrodes in 40 ms. The pixels at the vertical radius of the pipe cross section are shown for each image. c. Transverse representation of 9 of the 156 reconstructed EIT images of the air bubble. The state of the bubble at different instances is clearly seen in the nine tomograms.

### C. Dynamic Two-Phase Flows

An experiment were set up on a horizontal water/air two-phase flow rig to test the performances of the ONE-SHOT method in the context of dynamic two-phase flows.

Fig. 8a. represents the EIT sensor plugged in the multiphase rig in University of South-eastern Norway, Campus Porsgrunn. The experiment consists in a water flow mass of 60 kg/min flowing in a pipe of diameter 51 mm. A tiny air flow of 0.01 kg/min is introduced in the pipe, resulting in small bubbles flowing at the velocity of about 1 m/s.

The DAQ controller and the PCB are connected to an EIT sensor of diameter 51 mm which contains a set of 16 electrodes of surface 1 cm × 0.5 cm. The EIT sensor is plugged in the flow rig. Each of the 120 positive and negative excitation signals has an amplitude of 0.2 mV. Their frequencies vary from 31 kHz to 499 kHz. The FFT in each electrode channel is computed over 256 data points at the rate  $f_{acq} = 1$  MS/s. Therefore, each data frame contains 1920 measurement data points. The frames are recorded at the rate of 3906 fps.

A series of images (Fig. 8b. and c.) are reconstructed from the inhomogeneous dynamic flow with the one-step least-squares iterative reconstruction method as in Sec. VII-A and Sec. VII-B. The ONE-SHOT method successfully measured 156 frames of the bubble passing the cross-section of the electrodes in 40 ms.

### D. Signal-to-Noise Ratio Analysis

The SNR of a signal magnitude  $M_n(k)$  measured at a given electrode  $n$  and tagged with a given frequency  $k$  is defined as follows:

$$SNR_n(k) = \log_{10} \left[ \frac{\sum_{\lambda} [M_n(k)]_{\lambda}/R}{\sum_{\lambda} ([M_n(k)]_{\lambda}/R)^2 + \sum_{\lambda} ([M_n^0(k)]_{\lambda}/R)^2} \right] \quad (13)$$

where  $M_n^0(k)$  is an experimentally measured set of voltage magnitude, without any excitation to identify the noise spectrum [20].

The SNR of the raw signal magnitude is 69.1 dB in the excitation electrode channel for  $f_k = f_1$  when averaging the signal from  $\lambda = 20$  samples. In a non-excited channel, the signal is  $O(0.1)$  weaker, resulting in a SNR of about 60 dB depending on the signal magnitude. At the highest frequency  $f_k = f_{120} = 468.7$  kHz, the SNR is 55.6 dB in the excitation channel.

## VIII. SPECTRAL ANALYSIS

The experimental datasets presented in Sec. VII contain different magnitudes for the same excitation amplitude of all signals. The reason is that the impedance  $Z$  of a material depends on the frequency of the electrical excitation  $Z = Z(f)$ . We setup an experiment to measure the water impedance dependency on the frequency to explain the trend in the data from multifrequency excitations.

In the following study, opposite electrodes ( $E_1$  and  $E_9$ ) are selected as the source and drain of an imposed alternative electrical potential. The magnitudes and phase responses measured from several NaCl solutions at various conductivities and excitation frequencies are investigated.

### A. Impedance Magnitude

As in Fig. 9, the impedance in the low frequency domain ( $f \leq 10^2$  Hz) is influenced by the electrode-electrolyte interface [8]. The response to an electric potential is the formation of a double ion layer, essentially acting as a dielectric. One layer of ions forms from the electrons that are absorbed or emitted by the electrode. The ions of the other layer are attracted to the surface due to the Coulomb force. The phenomenon disappears when the frequency increases.

At the medium frequencies ( $10^2$  Hz  $\leq f \leq 10^4$  Hz), the impedance seems independent to the frequency. In the frame of the ONE-SHOT method, the generation of a full set of signal frequencies within this range can be a solution to obtain a homogeneous magnitude response. However, the data frame acquisition rate is significantly reduced in this situation.

At higher frequencies ( $f \geq 10^4$  Hz) the impedance shows an increasing dependency on frequency. This results in a

TABLE I

COMPARISON OF THE PERFORMANCES OF THE ONE-SHOT METHOD WITH THREE EXISTING HIGH-RATE EIT SYSTEMS BASED ON TDM.

System	$f_{acq}$ (MS/s)	$n_e$	Data size	NMS	Data frame acquisition rate (fps)	Excitation frequency (kHz)	SNR (dB)
Phantom [10], 2008	1	64	$15 \times 63$	172 652	182.7	1 to 10 000	65.5 to 98.6
Phantom [11], 2015	10	16	$16 \times 16$	28 160	110	97.65	90
ProME-T [15], 2017	2	16	$16 \times 120$	1 599 360	833	15	60
ONE-SHOT, 2019	1	16	$16 \times 120$	7 500 000	3 906.3	4 to 469	55.6 to 69.1

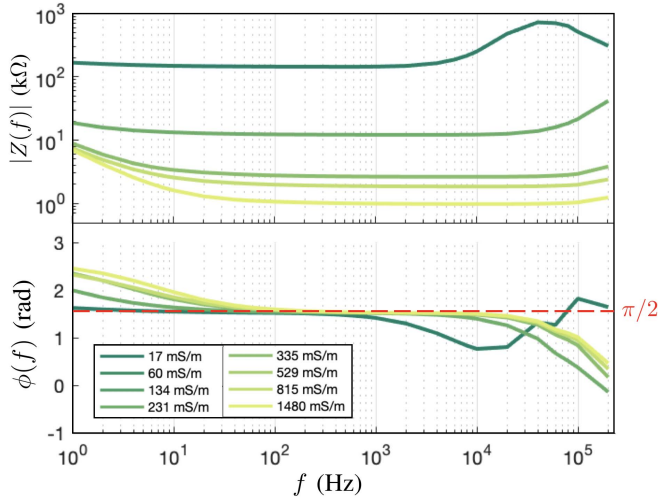


Fig. 9. Bode diagram of homogenous NaCl solutions of different electrical conductivities. The impedance on the top and the phase on the bottom are represented as functions of the imposed signal frequency.

weaker response in amplitude in the high harmonic range for the same conductivity change in the system. Investigations are ongoing for calibrating the amplitude of the generated sinusoidal signals to have a similar response for all the harmonics considered for a future generation of DAQ systems based on the ONE-SHOT method.

### B. Phase Shift

Concerning the phase shift, the results in Fig. 9 shows that  $|\phi_n| \gtrsim \pi/2$  on most of the spectral domain. As discussed in Sec. VI-C, the sign of the magnitude data points cannot be ascertained from (10). For this reason, the usage of the sign matrix as given in (12) is justified.

## IX. CONTACT IMPEDANCE

In TDM based EIT, the effects of contact impedance can be neglected by assuming the current in the measurement channel to be negligible. In practice, this is true since the data obtained from the pair of excitation electrodes are always discarded. Under these assumptions, the ideal circuit model is used for the ensuing calculations.

On the other hand, in the ONE-SHOT method each measurement channel is subject to the full set of simultaneous excitations. It is on an a priori basis impossible to use the ideal circuit model since every measurement electrode is used

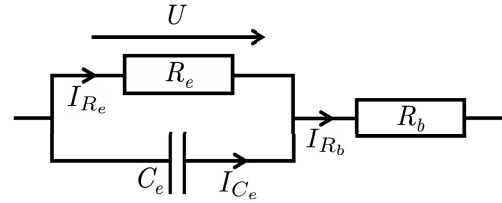


Fig. 10. Electrode model composed of a charge transfer resistance  $R_e$ , a double layer capacitance  $C_e$  and a bulk resistance  $R_b$ .

for excitation at the same time. The demodulation process occurs in different frequency bands, it ensures that a specific measurement associated with a specific channel with the associated frequency band is free from contact impedance effects due to currents at frequencies not in the bandwidth of the actual measurement channel.

A more accurate definition of the problem follows. The effects of the contact impedance from a frequency band to another can be investigated based on the electrode model described in [12], [54]. The equivalent circuit shown in Figure 10 neglects the contribution of the diffusion layer impedance. The combination of the charge transfer resistance  $R_e$  and the double layer capacitance  $C_e$  contributes to the capacitive effects. It results in a phase shift between the applied current and the electrode potential.

The total impedance according to the electrode model is:

$$\begin{aligned} Z(\omega) &= \left( \frac{1}{R_e} + i\omega C_e \right)^{-1} + R_b \\ &= \left( \frac{R_e}{1 + (\omega C_e R_e)^2} + R_b \right) - i \frac{\omega C_e R_e}{1 + (\omega C_e R_e)^2}. \end{aligned} \quad (14)$$

With the time constant associated with the electrode,  $\tau_0 = R_e C_e$ , when the angular frequency  $\omega \sim \omega_0 = 1/\tau_0$ , i.e.  $\omega R_e C_e \sim 1$ , the phase shift between the applied current and the electrode voltage is significant ( $\sim \pi/4$ ) for  $R_e \gg R_b$ . The currents follows:

$$\begin{cases} I_{C_e} = C_e dU/dt, \\ I_{R_e} = U/R_e, \\ I_{R_b} = I_{R_e} + I_{C_e} = I. \end{cases} \quad (15)$$

By applying a multifrequency AC current of the form:

$$\tilde{I} = I_0 \sum_{k=1}^{n_e-1} \sin(2\pi f_k t) \quad (16)$$

The total impedance becomes a function of the form:

$$\tilde{Z}(\omega, f_1, f_2, \dots, f_{n_e-1}) = \sum_{k=1}^{n_e-1} \tilde{Z}(\omega, f_k) + \tilde{\zeta}(\omega, f_1, f_2, \dots, f_{n_e-1}) \quad (17)$$

where  $\tilde{\zeta}(\omega, f_1, f_2, \dots, f_{n_e-1})$  is a cross-frequency term. In our model, we make the hypothesis that  $\tilde{\zeta}(\omega, f_1, f_2, \dots, f_{n_e-1}) \ll \tilde{Z}(\omega, f_k)$  for any  $1 \ll k \ll n_e - 1$  and  $k \in \mathbb{N}$ . The quality of the images reconstructed by the ONE-SHOT method is an indicator that the hypothesis is valid in the scope of our applications.

## X. CONCLUSION

This article presents a complete implementation of simultaneous excitations and measurements using a multifrequency strategy for high-speed EIT, based on the ONE-SHOT method with the essential details of hardware and software using LabVIEW and NI-modules.

Table I shows the performances of the ONE-SHOT method with a number of existing high-rate EIT systems. The description of the different hardware systems contains several characteristics that have to be considered in spite of the data frame rates, including the Number of Measurements per Second (NMS).

- The AI sampling frequency directly affects the data frame rate.
- The data size is an important factor to be maximised to improve the conditioning of the inverse problem.
- The noise also directly impacts the image quality. The noise is the value currently measured in a partially-shielded DAQ prototype.

Future implementations, especially including an improved PCB design, will result in better SNR.

Three prospects for the development of the method are currently under investigation.

- A new hardware system for 32 electrodes ONE-SHOT method is under development. The corresponding full implementation requires the simultaneous excitation and measurement of 992 signals at 496 frequencies.
- Another strategy is to generate electric excitation patterns that are orthogonal potential functions, defined on the boundary of the probed medium. The benefits of this method are smaller set of frequencies used in the excitation and smaller data size while keeping a complete set of measurements for image reconstruction.
- The implementation of an online reconstruction algorithm on the FPGA is proposed in [55].

Finally, further work concerns the quantification of the cross-frequency impedance term  $\tilde{\zeta}(\omega, f_1, f_2, \dots, f_{n_e-1})$  compared to the impedance  $\tilde{Z}(\omega, f_k)$  in the analysis of contact impedance with multifrequency current excitations.

## NOMENCLATURE

AI Analog Input  
AO Analog Output

BRAM	Block Random Access Memory
DAQ	Data Acquisition
DDS	Direct Digital Synthesis
DMA	Direct Memory Access
ECT	Electrical Capacitance Tomography
EIT	Electrical Impedance Tomography
FDM	Frequency-Division Multiplexing
FFT	Fast Fourier Transform
FIFO	First-In-First-Out
FPGA	Field Programmable Gate Array
fps	frames per seconds
I16	16-bits Integer
IRQ	An Interrupt Request
LUT	Look-Up-Table
MS/s	Mega Samples per second
NMS	Number of Measurements per Second
ONE-SHOT	One Excitation for Simultaneous High-speed Operation Tomography
PCB	Printed Circuit Board
RT	Real Time
SNR	Signal-to-Noise Ratio
TDM	Time-Division Multiplexing
U16, U32, U64	16, 32, 64-bits Unsigned integer

## ACKNOWLEDGMENT

Mathieu Darnajou and Chunhui Dang are Ph.D. students in École Centrale de Marseille and Aix Marseille Université. Multiphase experimental campaign involving a multi-modal sensor suite including the EIT and ECT was done in the process lab at University of South-eastern Norway with the help of Senior Engineer Fredrik Hansen and master student Aleksander Tokle Poevrud.

## REFERENCES

- [1] W. R. Breckon and M. K. Pidcock, "Mathematical aspects of impedance imaging," *Clin. Phys. Physiol. Meas.*, vol. 8, no. 4A, pp. 77–84, Nov. 1987, doi: [10.1088/0143-0815/8/4a/010](https://doi.org/10.1088/0143-0815/8/4a/010).
- [2] M. Cheney, D. Isaacson, and J. C. Newell, "Electrical impedance tomography," *SIAM Rev.*, vol. 41, no. 1, pp. 85–101, Jan. 1999, doi: [10.1137/S0036144598333613](https://doi.org/10.1137/S0036144598333613).
- [3] L. Borcea, "Electrical impedance tomography," *Inverse Problems*, vol. 18, no. 6, pp. R99–R136, Dec. 2002, doi: [10.1088/0266-5611/18/6/201](https://doi.org/10.1088/0266-5611/18/6/201).
- [4] M. Hanke and M. Brühl, "Recent progress in electrical impedance tomography," *Inverse Problems*, vol. 19, no. 6, pp. S65–S90, Dec. 2003, doi: [10.1088/0266-5611/19/6/055](https://doi.org/10.1088/0266-5611/19/6/055).
- [5] M. Darnajou, C. Dang, G. Ricciardi, S. Bourennane, C. Bellis, and H. Schmidt, "The design of electrical impedance tomography detectors in nuclear industry," in *Proc. World Congr. Ind. Process Tomogr.*, 2017, pp. 457–465.
- [6] P. Kauppinen, J. Hyttinen, and J. Malmivuo, "Sensitivity distribution visualizations of impedance tomography measurement strategies," *Int. J. Bioelectromagn.*, vol. 8, pp. VII-1–VII-9, Jan. 2006.
- [7] C. Dang, M. Darnajou, C. Bellis, G. Ricciardi, H. Schmidt, and S. Bourennane, "Numerical and experimental analysis of the correlation between EIT data eigenvalues and two-phase flow phase fraction," *Meas. Sci. Technol.*, vol. 31, no. 1, Jan. 2020, Art. no. 015302, doi: [10.1088/1361-6501/ab3d63](https://doi.org/10.1088/1361-6501/ab3d63).
- [8] A. Dupre, G. Ricciardi, S. Bourennane, and S. Mylvaganam, "Electrical capacitance-based flow regimes identification—multiphase experiments and sensor modeling," *IEEE Sensors J.*, vol. 17, no. 24, pp. 8117–8128, Dec. 2017, doi: [10.1109/JSEN.2017.2707659](https://doi.org/10.1109/JSEN.2017.2707659).

- [9] G. Ricciardi, M. J. Pettigrew, and N. W. Mureithi, "Fluidelastic instability in a normal triangular tube bundle subjected to air-water cross-flow," *J. Pressure Vessel Technol.*, vol. 133, no. 6, Dec. 2011, doi: [10.1115/1.4004562](https://doi.org/10.1115/1.4004562).
- [10] R. J. Halter, A. Hartov, and K. D. Paulsen, "A broadband high-frequency electrical impedance tomography system for breast imaging," *IEEE Trans. Biomed. Eng.*, vol. 55, no. 2, pp. 650–659, Feb. 2008, doi: [10.1109/TBME.2007.903516](https://doi.org/10.1109/TBME.2007.903516).
- [11] S. Khan, P. Manwaring, A. Borsic, and R. Halter, "FPGA-based voltage and current dual drive system for high frame rate electrical impedance tomography," *IEEE Trans. Med. Imag.*, vol. 34, no. 4, pp. 888–901, Apr. 2015, doi: [10.1109/TMI.2014.2367315](https://doi.org/10.1109/TMI.2014.2367315).
- [12] B. Wang, H. Ji, Z. Huang, and H. Li, "A high-speed data acquisition system for ECT based on the differential sampling method," *IEEE Sensors J.*, vol. 5, no. 2, pp. 308–312, Apr. 2005, doi: [10.1109/JSEN.2004.842627](https://doi.org/10.1109/JSEN.2004.842627).
- [13] Z. Cui, H. Wang, Z. Chen, Y. Xu, and W. Yang, "A high-performance digital system for electrical capacitance tomography," *Meas. Sci. Technol.*, vol. 22, no. 5, May 2011, Art. no. 055503, doi: [10.1088/0957-0233/22/5/055503](https://doi.org/10.1088/0957-0233/22/5/055503).
- [14] D. P. Morales, N. López-Ruiz, E. Castillo, A. García, and A. Martínez-Olmos, "Adaptive ECT system based on reconfigurable electronics," *Measurement*, vol. 74, pp. 238–245, Oct. 2015, doi: [10.1016/j.measurement.2015.07.035](https://doi.org/10.1016/j.measurement.2015.07.035).
- [15] A. Dupré, "Electrical impedance tomography for void fraction measurements of harsh two-phase flows: Prototype development and reconstruction techniques," Ph.D. dissertation, École centrale de Marseille, Marseille, France, 2017. [Online]. Available: <https://tel.archives-ouvertes.fr/tel-01656977>
- [16] Y. Granot, A. Ivorra, and B. Rubinsky, "Frequency-division multiplexing for electrical impedance tomography in biomedical applications," *Int. J. Biomed. Imag.*, vol. 2007, pp. 1–9, 2007.
- [17] T. Dowrick and D. Holder, "Phase division multiplexed EIT for enhanced temporal resolution," *Physiol. Meas.*, vol. 39, no. 3, Mar. 2018, Art. no. 034005, doi: [10.1088/1361-6579/aaad59](https://doi.org/10.1088/1361-6579/aaad59).
- [18] J. R. Mager, S. D. Sibley, T. R. Beckman, T. A. Kellogg, and C. P. Earthman, "Multifrequency bioelectrical impedance analysis and bioimpedance spectroscopy for monitoring fluid and body cell mass changes after gastric bypass surgery," *Clin. Nutrition*, vol. 27, no. 6, pp. 832–841, Dec. 2008, doi: [10.1016/j.clnu.2008.06.007](https://doi.org/10.1016/j.clnu.2008.06.007).
- [19] A. Dupré and S. Mylvaganam, "A simultaneous and continuous excitation method for high-speed electrical impedance tomography with reduced transients and noise sensitivity," *Sensors*, vol. 18, no. 4, p. 1013, Mar. 2018, doi: [10.3390/s18041013](https://doi.org/10.3390/s18041013).
- [20] M. Darnajou, A. Dupré, C. Dang, G. Ricciardi, S. Bourennane, and C. Bellis, "On the implementation of simultaneous multi-frequency excitations and measurements for electrical impedance tomography," *Sensors*, vol. 19, no. 17, p. 3679, Aug. 2019, doi: [10.3390/s19173679](https://doi.org/10.3390/s19173679).
- [21] K. S. Osterman, T. E. Kerner, D. B. Williams, A. Hartov, S. P. Poplack, and K. D. Paulsen, "Multifrequency electrical impedance imaging: Preliminary in vivo experience in breast," *Physiol. Meas.*, vol. 21, no. 1, pp. 99–109, Feb. 2000, doi: [10.1088/0967-3334/21/1/313](https://doi.org/10.1088/0967-3334/21/1/313).
- [22] H. Wi, H. Sohal, A. L. McEwan, E. Je Woo, and T. I. Oh, "Multi-frequency electrical impedance tomography system with automatic self-calibration for long-term monitoring," *IEEE Trans. Biomed. Circuits Syst.*, vol. 8, no. 1, pp. 119–128, Feb. 2014, doi: [10.1109/TBCAS.2013.2256785](https://doi.org/10.1109/TBCAS.2013.2256785).
- [23] E. Malone, G. Sato Dos Santos, D. Holder, and S. Arridge, "Multi-frequency electrical impedance tomography using spectral constraints," *IEEE Trans. Med. Imag.*, vol. 33, no. 2, pp. 340–350, Feb. 2014, doi: [10.1109/TMI.2013.2284966](https://doi.org/10.1109/TMI.2013.2284966).
- [24] Z. Zhou *et al.*, "Multifrequency electrical impedance tomography with total variation regularization," *Physiol. Meas.*, vol. 36, no. 9, pp. 1943–1961, Sep. 2015, doi: [10.1088/0967-3334/36/9/1943](https://doi.org/10.1088/0967-3334/36/9/1943).
- [25] Y. Yang and J. Jia, "A multi-frequency electrical impedance tomography system for real-time 2D and 3D imaging," *Rev. Scientific Instrum.*, vol. 88, no. 8, Aug. 2017, Art. no. 085110, doi: [10.1063/1.4999359](https://doi.org/10.1063/1.4999359).
- [26] N. Goren *et al.*, "Multi-frequency electrical impedance tomography and neuroimaging data in stroke patients," *Scientific Data*, vol. 5, no. 1, Dec. 2018, Art. no. 180112, doi: [10.1038/sdata.2018.112](https://doi.org/10.1038/sdata.2018.112).
- [27] H. Wang, S. Xin, and X. Zhang, "New progress of the digital electrical capacitance tomography system for gas/liquid two phase flow," in *Proc. IEEE Int. Workshop Imag. Syst. Techn.*, May 2009, pp. 37–40, doi: [10.1109/IST.2009.5071598](https://doi.org/10.1109/IST.2009.5071598).
- [28] Y. Yang and L. Peng, "A configurable electrical capacitance tomography system using a combining electrode strategy," *Meas. Sci. Technol.*, vol. 24, no. 7, Jul. 2013, Art. no. 074005, doi: [10.1088/0957-0233/24/7/074005](https://doi.org/10.1088/0957-0233/24/7/074005).
- [29] M. Zhang and M. Soleimani, "Simultaneous reconstruction of permittivity and conductivity using multi-frequency admittance measurement in electrical capacitance tomography," *Meas. Sci. Technol.*, vol. 27, no. 2, Feb. 2016, Art. no. 025405, doi: [10.1088/0957-0233/27/2/025405](https://doi.org/10.1088/0957-0233/27/2/025405).
- [30] Y. Yang, L. Peng, and J. Jia, "A novel multi-electrode sensing strategy for electrical capacitance tomography with ultra-low dynamic range," *Flow Meas. Instrum.*, vol. 53, pp. 67–79, Mar. 2017, doi: [10.1016/j.flowmeasinst.2016.05.005](https://doi.org/10.1016/j.flowmeasinst.2016.05.005).
- [31] R.-S. Wu, F. V. Araújo, and L.-J. Huang, "Multifrequency backscattering tomography for constant and vertically varying backgrounds," *Int. J. Imag. Syst. Technol.*, vol. 5, no. 1, pp. 7–21, 1994, doi: [10.1002/ima.1850050103](https://doi.org/10.1002/ima.1850050103).
- [32] H. Scharfetter, A. Köstinger, and S. Issa, "Hardware for quasi-single-shot multifrequency magnetic induction tomography (MIT): The graz Mk2 system," *Physiol. Meas.*, vol. 29, no. 6, pp. S431–S443, Jun. 2008, doi: [10.1088/0967-3334/29/6/s36](https://doi.org/10.1088/0967-3334/29/6/s36).
- [33] C. Donadio, A. B. Halim, F. Caprio, G. Grassi, B. Khedr, and M. Mazzantini, "Single- and multi-frequency bioelectrical impedance analyses to analyse body composition in maintenance haemodialysis patients: Comparison with dual-energy X-ray absorptiometry," *Physiol. Meas.*, vol. 29, no. 6, pp. S517–S524, Jun. 2008, doi: [10.1088/0967-3334/29/6/s43](https://doi.org/10.1088/0967-3334/29/6/s43).
- [34] R. N. Baumgartner, W. C. Chumlea, and A. F. Roche, "Estimation of body composition from bioelectric impedance of body segments," *Amer. J. Clin. Nutrition*, vol. 50, no. 2, pp. 221–226, Aug. 1989, doi: [10.1093/ajcn/50.2.221](https://doi.org/10.1093/ajcn/50.2.221).
- [35] J. A. Salmi, "Body composition assessment with segmental multi-frequency bioimpedance method," M.S. thesis, Dept. Physiol., Univ. Kuopio, Kuopio, Finland, 2003.
- [36] Z. Cui, H. Wang, Z. Chen, Y. Xu, and W. Yang, "A high-performance digital system for electrical capacitance tomography," *Meas. Sci. Technol.*, vol. 22, no. 5, May 2011, Art. no. 055503.
- [37] S. S. Palle *et al.*, "Multi-frequency bioelectrical impedance analysis (BIA) compared to magnetic resonance imaging (MRI) for estimation of fat-free mass in colorectal cancer patients treated with chemotherapy," *Clin. Nutrition ESPEN*, vol. 16, pp. 8–15, Dec. 2016, doi: [10.1016/j.clnesp.2016.09.003](https://doi.org/10.1016/j.clnesp.2016.09.003).
- [38] H. Ammari, F. Triki, and C.-H. Tsou, "Numerical determination of anomalies in multifrequency electrical impedance tomography," *Eur. J. Appl. Math.*, vol. 30, no. 3, pp. 481–504, Jun. 2019.
- [39] D. Lockstone, "20-frequency division multiplexing," in *Telecommunications Engineer's Reference Book*, F. Mazda, Ed. London, U.K.: Heinemann, 1993, pp. 20-1–20-22. [Online]. Available: <http://www.sciencedirect.com/science/article/pii/B9780750611626500265>
- [40] J. Max and J. L. Lacoume, *Méthodes et Techniques de Traitement du Signal*, 5th ed. Grenoble, France: Sciences Sup, Dunod, 2004.
- [41] Á. Quirós-Olozábal, J.-J. González-de-la-Rosa, M.-Á. Cifredo-Chacón, and J.-M. Sierra-Fernández, "A novel FPGA-based system for real-time calculation of the spectral kurtosis: A prospective application to harmonic detection," *Measurement*, vol. 86, pp. 101–113, May 2016, doi: [10.1016/j.measurement.2016.02.031](https://doi.org/10.1016/j.measurement.2016.02.031).
- [42] National Instruments. (Aug. 2016). *Embedded CompactRIO Controller with Real-Time Processor Reconfigurable FPGA*. [Online]. Available: <http://www.ni.com/pdf/manuals/375697d>
- [43] National Instruments. (Sep. 2017). *1 MS/s/ch Simultaneous, ±10 V, 6-Channel C Series Voltage Output Module*. [Online]. Available: <http://www.ni.com/pdf/manuals/377139a>
- [44] National Instruments. (Feb. 2016). *4 AI, ±10 V, 16 Bit, 1 MS/s/ch Simultaneous*. [Online]. Available: <http://www.ni.com/pdf/manuals/374223a>
- [45] R. S. Correa and J. P. David, "Ultra-low latency communication channels for FPGA-based HPC cluster," *Integration*, vol. 63, pp. 41–55, Sep. 2018. [Online]. Available: <http://www.sciencedirect.com/science/article/pii/S0167926017303966>, doi: [10.1016/j.vlsi.2018.05.005](https://doi.org/10.1016/j.vlsi.2018.05.005).
- [46] J. U. Kidav, N. M. Sivamangai, M. P. Pillai, and S. Raja, "Architecture and FPGA prototype of cycle stealing DMA array signal processor for ultrasound sector imaging systems," *Microprocess. Microsyst.*, vol. 64, pp. 53–72, Feb. 2019. [Online]. Available: <http://www.sciencedirect.com/science/article/pii/S0141933118302540>, doi: [10.1016/j.micpro.2018.10.005](https://doi.org/10.1016/j.micpro.2018.10.005).

- [47] L. Yang, F. Li, Z. Xiong, G. Shi, Y. Niu, and R. Li, "Single-shot dense depth sensing with frequency-division multiplexing fringe projection," *J. Vis. Commun. Image Represent.*, vol. 46, pp. 139–149, Jul. 2017. [Online]. Available: <http://www.sciencedirect.com/science/article/pii/S104732031730086X>, doi: [10.1016/j.jvcir.2017.03.018](https://doi.org/10.1016/j.jvcir.2017.03.018).
- [48] National Instruments. (Jun. 2019). *Kintex-7 FPGAs Data Sheet: DC AC Switching Characteristics*. [Online]. Available: [https://www.xilinx.com/support/documentation/data\\_sheets/ds182\\_Kintex\\_7\\_Data\\_Sheet.pdf](https://www.xilinx.com/support/documentation/data_sheets/ds182_Kintex_7_Data_Sheet.pdf)
- [49] M. Wang, Y. Ma, N. Holliday, Y. Dai, R. A. Williams, and G. Lucas, "A high-performance EIT system," *IEEE Sensors J.*, vol. 5, no. 2, pp. 289–299, Apr. 2005, doi: [10.1109/JSEN.2005.843904](https://doi.org/10.1109/JSEN.2005.843904).
- [50] A. J. Wilkinson, E. W. Randall, J. J. Cilliers, D. R. Durrett, T. Naidoo, and T. Long, "A 1000-measurement frames/second ERT data capture system with real-time visualization," *IEEE Sensors J.*, vol. 5, no. 2, pp. 300–307, Apr. 2005, doi: [10.1109/JSEN.2004.842445](https://doi.org/10.1109/JSEN.2004.842445).
- [51] A. Dupre, G. Ricciardi, and S. Bourennane, "Novel approach for analysis and design of high-speed electrical impedance tomographic system for void fraction measurements in fast two-phase flows," *IEEE Sensors J.*, vol. 17, no. 14, pp. 4472–4482, Jul. 2017, doi: [10.1109/JSEN.2017.2707665](https://doi.org/10.1109/JSEN.2017.2707665).
- [52] T. J. Yorkey, J. G. Webster, and W. J. Tompkins, "Comparing reconstruction algorithms for electrical impedance tomography," *IEEE Trans. Biomed. Eng.*, vol. BME-34, no. 11, pp. 843–852, Nov. 1987, doi: [10.1109/TBME.1987.326032](https://doi.org/10.1109/TBME.1987.326032).
- [53] M. C. Kim, S. Kim, K. Y. Kim, and Y. J. Lee, "Regularization methods in electrical impedance tomography technique for the two-phase flow visualization," *Int. Commun. Heat Mass Transf.*, vol. 28, no. 6, pp. 773–782, Aug. 2001. [Online]. Available: <http://www.sciencedirect.com/science/article/pii/S0735193301002810>, doi: [10.1016/S0735-1933\(01\)00281-0](https://doi.org/10.1016/S0735-1933(01)00281-0).
- [54] S. Khan, A. Borsic, P. Manwaring, A. Hartov, and R. Halter, "FPGA based high speed data acquisition system for electrical impedance tomography," *J. Phys., Conf. Ser.*, vol. 434, Apr. 2013, Art. no. 012081, doi: [10.1088/1742-6596/434/1/012081](https://doi.org/10.1088/1742-6596/434/1/012081).
- [55] Y. Zhou and X. Li, "A real-time EIT imaging system based on the split augmented lagrangian shrinkage algorithm," *Measurement*, vol. 110, pp. 27–42, Nov. 2017, doi: [10.1016/j.measurement.2017.06.018](https://doi.org/10.1016/j.measurement.2017.06.018).
- [56] Sintef. (2020). *SAM*. [Online]. Available: <https://www.sintef.no/en/projects/sam-self-adapting-model-based-system-for-process-autonomy/>